A Novel Force Modeling Scheme for Needle Insertion Using Multiple Kalman Filters

Ali Asadian, *Student Member, IEEE*, Mehrdad R. Kermani, *Member, IEEE*, and Rajni V. Patel, *Fellow, IEEE*

***Abstract*—In this paper, the interaction force between a surgical needle and soft tissue is studied. The force is modeled using a novel nonlinear dynamic model. Encouraged by the LuGre model for representing friction forces, the proposed model captures all stages of needle–tissue interaction, including puncture, cutting, and friction forces. An estimation algorithm for identifying the parameters of the model is presented. This online approach, which is based on sequential extended Kalman filtering, enables us to characterize the total contact force using an efficient mathematical model. The algorithm compares the axial force measured at the needle base with its expected value and then adapts the model parameters to represent the actual interaction force. While the nature of this problem is very complex, the use of multiple Kalman filters makes the system highly adaptable for capturing the force evolution during an interventional procedure in standard operating conditions. To evaluate the performance of our model, experiments were performed on artificial phantoms.**

***Index Terms*—Computer-assisted surgery, force modeling, Kalman filtering, needle insertion, needle–tissue interaction.**

I. Introduction

MEDICAL intervention using surgical needles is a common minimally invasive procedure. Flexible needles can facilitate curved trajectories and are utilized for localized drug delivery, radioactive seed placement, neurosurgery, ablation, or tissue biopsy, particularly in regions that are difficult to access or in deep zones. In this context, robot-assisted needle steering, which is intended to guide the needle to the targeted locations inside soft tissue, has become an active research area [1]. In this respect, positioning inaccuracy originates from a variety of factors, such as the following: 1) soft tissue deformation; 2) bending mechanics as a result of tissue–needle interaction; 3) inhomogeneity, nonlinear viscoelasticity, and anisotropy of real organic tissue; 4) target movement due to respiration, heartbeat, or similar artifacts; and, finally, 5) tiny anatomic structures which could not be easily detected by conventional imaging modalities.

In therapeutic procedures, if applicable and possible, increasing the amount of steering may improve the accuracy of diagnosis. This is restricted by the amount of steering that can be achieved once the needle is inserted, and usually, the needle divergence from its desired path degrades the effectiveness of the diagnosis or treatment. In this regard, the actual path can be directly linked to the force signals experienced by the needle during penetration. Thus, accurate modeling is the first step toward developing a precise and effective trajectory planning scenario. Ultimately, the force model can be employed either in fully autonomous motion planning [2], [3] or in a force feedback teleoperation scheme, either to assist a surgeon or as a training simulator [4]. High-fidelity simulators should have the capability to provide realistic haptic perception to the user. In semiautonomous steering, where the surgeon remains in the loop, a force control approach allows the slave system to insert the needle to the desired penetration depth and also gives the operator a realistic sense of needle–tissue interaction so that the operator can take further actions.

In case of percutaneous interventions, understanding the contact mechanism between the surgical needle and organs is a complex task. Indeed, environmental features including soft tissue dynamics are important to design the robot-assisted control strategy. During the needle–tissue interaction, prepuncture corresponds to a viscoelastic behavior, and postpuncture interaction forces are due to the combined effects of cutting force, friction, and tissue relaxation. Finally, during retraction or needle withdrawal, friction is the sole interactive force [5]. Identification of the associated properties can be rendered by employing adequate modalities. For instance, detection of abrupt changes in successive layers is captured by a haptic device or a force/torque sensor. Nevertheless, characterization of the needle–tissue contact forces remains a challenge due to the following reasons [1], [8], [15].

1) The needle penetrates various layers of tissue, e.g., skin, fat, and muscles, and inhomogeneity, nonlinear viscoelasticity, and anisotropy of real organs suggest that the present force cannot be described by a simple structure.
2) Biomechanical properties are patient dependent and linked to the age, gender, disease stage, and needle geometry.

Manuscript received December 18, 2010; revised August 3, 2011; accepted August 4, 2011. Date of publication November 1, 2011; date of current version January 5, 2012. This research was supported by the Natural Sciences and Engineering Research Council (NSERC) of Canada under grants RGPIN-346166 (M.R. Kermani) and RGPIN-1345 (R.V. Patel). The work of A. Asadian was supported in part by the NSERC CREATE Program in Computer-Assisted Medical Interventions (CAMI) under Grant 371322-2009. A part of the work described in this paper was presented at the 32nd Annual International Conference of the IEEE Engineering in Medicine and Biology Society, Argentina, 2010. The Associate Editor coordinating the review process for this paper was Dr. Antonios Tsourdos.

A. Asadian and M. R. Kermani are with the Canadian Surgical Technologies and Advanced Robotics (CSTAR), Lawson Health Research Institute, London, ON, N6A 5A5, Canada, and with the Department of Electrical and Computer Engineering, The University of Western Ontario, London, ON, N6A 5B9, Canada (e-mail: aasadian@uwo.ca; mkermani@eng.uwo.ca).

R. V. Patel is with the Canadian Surgical Technologies and Advanced Robotics (CSTAR), Lawson Health Research Institute, London, ON, N6A 5A5, Canada. He is also with the Department of Electrical and Computer Engineering, The University of Western Ontario, London, ON, N6A 5B9, Canada, and also with the Department of Surgery, The University of Western Ontario, London, ON, N6A 4L6, Canada (e-mail: rvpatel@uwo.ca).

Color versions of one or more of the figures in this paper are available online at http://ieeexplore.ieee.org.

Digital Object Identifier 10.1109/TIM.2011.2169178

3) During insertion, the elementary contributions of the various layers are intermixed.

The main objective of this study is to identify needle–tissue properties during percutaneous interventions, thereby finding a mathematical model which mimics the translational force behavior. The outcome of this research will provide a means for characterizing the needle–tissue contact forces. The subject of needle insertion involves substantial biophysical variations to be characterized. Therefore, the physical modeling and direct estimation of these parameters may not be possible. To deal with this problem, we will introduce a nonlinear dynamic model that allows intraoperative data extraction of the force profile. Without explicit investigation of biomechanical aspects, in the following, we propose a recursive online estimation technique for system identification. The goal of the current work is to find a computationally feasible model that describes the relationship between the total axial force measured at the needle holder and the depth of insertion during both insertion and retraction in soft tissue. The proposed modeling and identification scheme enables us to tune the parameters according to the interaction properties. Consequently, any change in the mentioned properties which leads to a deviation in the insertion or retraction force can be intraoperatively captured by the model.

The outline of this paper is as follows. In Section II, the relevant studies in the area of needle–tissue force modeling are reviewed. Section III introduces the proposed nonlinear model that can describe needle–tissue interaction in the force domain. In Section IV, the employed recursive filtering method for system identification is explained, while in Section V, experimental results and discussions are given. Finally, Section VI presents conclusions and suggestions for future work.

II. Related Work and Our Motivation

As a pioneering work for force modeling in needle insertion, Okamura *et al.* [5] developed an empirical model for unilateral needle insertion force, which was a summation of capsule stiffness force, friction, and cutting forces. According to their model, the stiffness force occurs before the puncture of the capsule, while the friction and cutting forces occur right after the main puncture. In [6], interpretation of force features in conjunction with spectroscopic techniques was examined for a needle penetrating soft tissue with the aim of automatically identifying tissue type at the needle tip. Podder *et al.* [7] derived a statistical model to estimate the maximum force that the needle experienced during prostate brachytherapy. Insertion force data were collected to build their offline model based on the following: 1) patient-specific parameters, including prostate-specific antigen (PSA) level, body mass index (BMI), and prostate volume, and 2) procedure-specific criteria such as needle size and insertion velocity. They also quantified and measured *in vivo* insertion forces while implanting radioactive seeds in the prostate gland [8]. In this empirical study, the overall maximum measured forces on 18GA and 17GA needles with respect to velocity were compared.

DiMaio and Salcudean [9] illustrated a system for measuring the extent of planar polyvinyl chloride (PVC) phantom deformation during needle insertion. They investigated the insertion of a 17GA symmetric epidural needle and then estimated the forces applied to the needle shaft using a linear elastic finite-element method (FEM) and a vision system. Hing *et al.* [10] developed a system to predict soft tissue movement and involved force components using traditional FEM and ABAQUS software. Two C-arm fluoroscopes were used in this study to image fiducial markers and needle bending. Misra *et al.* [11] also explored the sensitivity of the axial force-to-tissue rupture toughness, tissue elasticity, as well as the bevel angle of the needle tip. Using both contact and cohesive zone models, they incorporated these physical parameters into an FEM-based model. Kobayashi *et al.* [12] developed another model including viscoelastic and nonlinear behavior based on detailed material properties. Using FEM, they validated the relationship between the needle displacement and the insertion force and evaluated its velocity dependence when puncture occurs.

Generally speaking, FEM is accurate and adequate for small linear elastic deformations. However, robot-assisted needle interventions usually deal with deep insertion depths. On the other hand, the numerical efficiency of this technique relies on the following: 1) the development of effective pre- and postprocessing; 2) the material parameters chosen; 3) the scale of deformation;and 4) the algorithm employed for solving the equations of continuum mechanics. Although researchers have focused efforts on optimizing FEM computational efficiency, it still does not allow for real-time complex simulations or intraoperative planning and control. This is due to the large system of equations involved as well as the frequent topological and boundary condition changes that occur as the needle moves into the tissue. In [13], a manual indentation technique and a handheld probe were proposed to estimate the biomechanical behavior of human body parts. This system can provide an initial setting for FEM-based approaches. Another weakness of FEM is the necessity of providing local deformations using markers or beads placed on the surface of or implanted into the material. The estimated movement of the beads is then used to validate the model. Obviously, it is difficult to employ this category of modeling methods in clinical conditions, particularly in the case of existing internal organs with complex geometries and boundary conditions.

Several studies have looked at alternative modeling methods. Viscoelastic properties of soft tissues can be represented by rheological models composed of serial and/or parallel combinations of springs (elastic elements) and dashpots (viscous elements). The spring–beam–damper model is the most common noncontinuum mechanics-based approach used for soft tissue modeling in small-scale motions. Despite its limited accuracy, it is efficient for real-time simulations and robot-assisted interventions. Using a set of local polynomials connected in serial finite segments, Yan *et al.* [14] presented an online estimator to approximate the depth-varying tissue parameters through force measurements. Keeping the insertion speed constant, the model was validated inserting an 18GA needle with a trihedral tip. Barbe *et al.* [15] developed another online scheme utilizing recursive least squares. It was then integrated to the Kelvin–Voigt viscoelastic interaction model with time-varying parameters to reconstruct the force evolution during insertion. Based on this analysis and possibly due to ignoring friction, an accurate

model could not be estimated in an online manner. Using the same interaction model, associated parallel spring and dashpot combinations were approximated by a set of piecewise linear functions at a constant insertion velocity [4].

Other important issues on modeling of tool–tissue interaction are still open for future research. Misra *et al.* [16] reviewed this matter with emphasis on surgical simulations. More aspects of the interaction from a biomechanics view have been reported in [17] and [18]. The former paper is an empirical study, and as observed, needle–tissue interaction and associated biomechanical properties are influenced by various factors. Thus, it can be impractical or impossible to measure or investigate the effect of the involved parameters separately.

Although it is well understood that incorporating explicit biomechanical features of soft tissue in estimation and modeling is part of an ideal solution, our intention is to focus on local force measurements to build a dynamic structure. It is worth mentioning that finding accurate physics behind the needle–tissue interaction model as a multifaceted problem is not deemed a priority here. Perhaps, the most significant impediment toward physically based modeling is the fact that the contact forces are influenced by complicated biophysical tissue behavior whose description using physical theories is still a challenge. In addition, the mechanism of cutting at the needle tip is not yet well formulated, and distributed friction along the needle shaft that affects the measurements has its own modeling complexities. These issues motivated us to study a non-physics-based approach, as presented in this paper.

To the best of our knowledge, no one has ever presented a compact and feasible model to capture both insertion and retraction forces. The importance of finding a computationally efficient model that can partly or fully embody the interaction properties is that it paves the path for focusing more on intraoperative model-based planning or teleoperation techniques that constitute our ultimate objectives in this body of work.

III. Reflecting Needle–Tissue Interaction in the Force Domain

Assuming a constant insertion velocity, the total translational force can be dynamically modeled as a function of insertion depth using the following nonlinear state-space model. Thus, the entire interaction including insertion and retraction phases can be described by a dynamic model, as proposed here.

The main motivation for this selection arose from the fact that the trend describing the total insertion force as a function of penetration depth is identical to the dynamic friction described by the LuGre model [19]. Replacing the velocity in the original LuGre model with the depth of insertion and modifying the measurement equation, the current model enables us to capture an approximation for the force pattern. In this setting, z is an internal state, and l stands for the depth of insertion acting as the model input. f also represents the axial force experienced by the needle, and it is the output of our single-state models as follows.

A. Model I

$$\begin{cases} \frac{dz}{dt} = l\left(\beta_0 - \frac{\sigma_0}{g(l)}z\right) \\ f = \sigma_0 z l + \text{sign}(\dot{l}) l \left\{\sigma_1 e^{-\alpha l}\left(\beta_0 - \frac{\sigma_0}{g(l)}z\right) + \sigma_2\right\} \end{cases} \tag{1}$$

where

$$g(l) = f_1 + f_2 e^{-\alpha l}. \tag{2}$$

As previously shown by the authors [20], the total force measured at the base is characterized by six parameters, namely, f_1, f_2, σ_0, σ_1, σ_2, and α, in model I. Collectively, the g function, which models the Stribeck effect in the traditional LuGre model, corresponds to the sharp drop in the insertion force once the main puncture occurs here. This function is defined by the following three parameters: f_1, f_2, and α. In (1), selecting a smaller value for σ_0 yields a bigger force peak and also a sharper force drop during the rupture. It has almost no impact on the retraction force profile. Changing the value of σ_1 results in the same effect during the insertion regime, but it also shapes the retraction axial force in the vicinity of the entry point. The value of σ_2 directly affects the steady-state value of the generated output and can remove the oscillation from the simulated force in the backward motion if the filter is properly tuned. β_0 is also a normalized constant.

Note that these parameters are not physically inspired, and thus, their role cannot be individually interpreted. Due to the same reason, as well as the combined effect of them on the generated force features, it is not possible to obtain the parameters separately. Instead, the recursive mechanism introduced in Section IV allows us to estimate the parameters, update the model, and reconstruct the force pattern during percutaneous interventions.

B. Model II

$$\begin{cases} \frac{dz}{dt} = l\left(\beta - \frac{\sigma_0}{g(l)}z\right) \\ f = \sigma_0 z l + \text{sign}(\dot{l}) l \left\{\sigma_1 e^{-\tilde{\alpha} l}\left(\beta - \frac{\sigma_0}{g(l)}z\right) + \sigma_2\right\} \end{cases} \tag{3}$$

where

$$g(l) = f_1 + \tilde{f}_2 e^{-\tilde{\alpha} l}. \tag{4}$$

As a reduced-order version of model I, model II is introduced in (3). In this structure, the unknown parameters α and f_2 are replaced with their estimated values provided by model I. The new values are named $\tilde{\alpha}$ and $\tilde{f}_2$, respectively. Here, a new varying parameter denoted by β is added to (1) to achieve a better overall accuracy. Model II is expected to suffer less from numerical issues compared to the previous state-space structure, and it will be discussed in Section V.

Compared to the existing models, in this study, no separation is made between axial force components, e.g., rupture, friction, and cutting forces, and the entire intervention, including insertion and retraction phases, is described by a single set of equations. Herein, the relaxation time has been

ignored, and the procedure is desired to be learned in an online scheme using a bank of Kalman filters in a switching process.

IV. Proposed Sequential Identification Procedure

Having selected one of the proposed models, the associated parameters are required to be experimentally identified. Generally speaking, the parameters that are hardly measurable but observable can be estimated using state-parameter estimation methods. Several studies and discussions have been reported in the literature on adaptive identification of the original LuGre model [19], [21], [22]. As a modification to this model, in this work, an estimator is realized using a joint state-parameter extended Kalman filter (EKF) technique. Details of the design of a conventional EKF as a widely accepted tool in estimation theory are discussed in [23]. It is assumed here that readers are familiar with discrete Kalman filtering.

To implement the joint state-parameter EKF, the original state vector (z) is augmented with new state variables (θ) which denote the unknown coefficients of the proposed model [24]. The dynamics of the augmented state is commonly assumed to be of random walk nature which is subject to zero-mean white noise perturbation (ζ). ζ is presumed to be uncorrelated with system noise (υ) and to have a positive definite variance [23].

A third-order Runge–Kutta algorithm is then employed to discretize the state-space representation of the system which includes the continuous force–depth model given in the previous section and the augmentative model. Let the discrete representation of the entire system at the kth instant be formulated as

$$\begin{cases} z^{k+1} = F(z^k, \theta^k, l^k) + \upsilon^k \\ \theta^{k+1} = \theta^k + \zeta^k \\ f^k = H(z^k, \theta^k, l^k) + \omega^k \end{cases} \tag{5}$$

where $\theta_{m\times 1}$ is the vector of model parameters, as introduced previously; $\upsilon_{1\times 1}$ and $\zeta_{m\times 1}$ are the process noises, while $\omega_{1\times 1}$ is the measurement noise. Thus, the stochastic dynamics of the interaction force transforms into

$$\begin{cases} \phi^{k+1} = \hat{F}(\phi^k, l^k) + \hat{\upsilon}^k \\ f^k = H(\phi^k, l^k) + \omega^k \end{cases} \tag{6}$$

in that $\hat{\upsilon}_{(m+1)\times 1}$ is the process noise of the new state vector (ϕ), which is written as

$$\phi^k_{(m+1)\times 1} \equiv \begin{pmatrix} z^k_{1\times 1} \\ \theta^k_{m\times 1} \end{pmatrix}.$$

The multiple EKF is then applied to estimate the augmented state vector which consists of both the original state variables and the augmentative state variables. This approach combines data asynchronously for use by EKFs in a switching mode. In other words, the multiple approach is to alternatively run multiple filters at which a subset of the states in the $\phi_{(m+1)\times 1}$ space is subjected to estimation and the rest of them are treated as known values [25]. The number of states estimated by a single EKF is chosen with respect to the observability properties of (6).

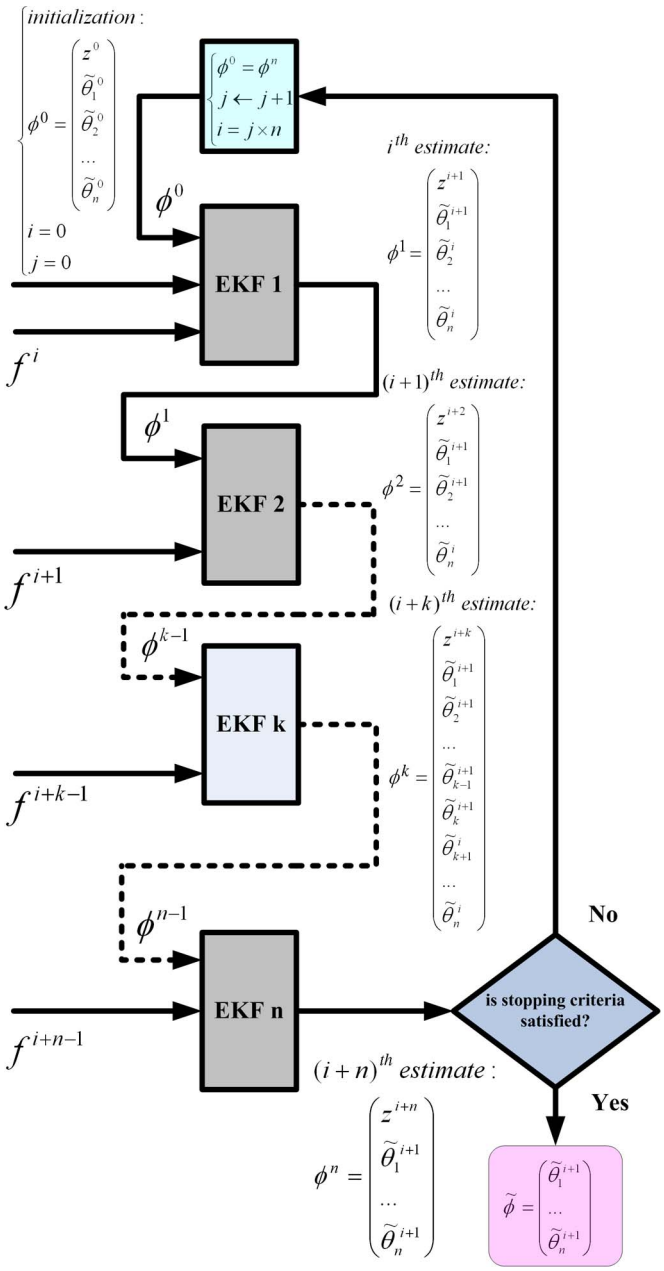

Fig. 1. Flowchart of the proposed sequential identification procedure.

Assume that $\tilde{\theta}_n$ $(1 \le n \le m)$ denotes a set of vectors, which tessellates $\theta_{m\times 1}$, i.e.,

$$\forall n, q\ (1 \le n, q \le m): \quad \tilde{\theta}_n \bigcap \tilde{\theta}_q = \emptyset$$
$$\bigcup_{n=1}^{m} \tilde{\theta}_n = \theta_{m\times 1}.$$

Each single joint EKF estimates the unknown vector of $\tilde{\theta}_n$ plus the internal state of the nonlinear dynamics (z) at the current step. Once the estimation is completed at the current iteration, the model is updated with the estimated values, i.e., the estimated vector is fed into the model, and then, the next filter in the queue is triggered. This procedure is followed iteratively until a narrow error bound as the stopping criterion is achieved. Fig. 1 shows the sequence of the estimation procedure as proposed in this study. Finally, $\tilde{\phi}$ represents the estimated

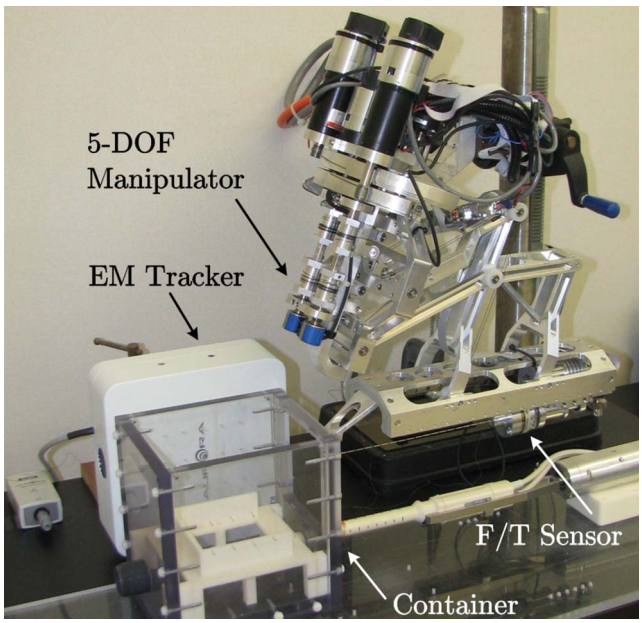

Fig. 2. View of our robotic system.

value for the unknown parameters. It should be noted that these parameters may have no physical interpretations.

V. Implementation and Experiments

A. Instrumentation

Experimental implementation of the proposed methodology was carried out on the state-of-the-art robotic system shown in Fig. 2, which has been fully designed and manufactured in our group for the primary application of prostate brachytherapy [26]. The 5-degree-of-freedom (DOF) manipulator can perform orientation, insertion, and rotation of the needle and linear motion of the plunger to drop radioactive seeds with an acceptable accuracy. A Nano43 6-DOF force/torque sensor (ATI Industrial Automation) that is attached to the needle holder and an Aurora electromagnetic (EM) tracker (Northern Digital, Inc.) are the external sensing devices for providing feedback signals. The control computer and the data capture computer were interfaced through a User Datagram Protocol (UDP) connection over Ethernet. A multithreaded application for position/velocity control, sensor readings, and communication was developed using Microsoft C++, MATLAB, and the QuaRC toolbox (Quanser Inc.). An Aurora 5-DOF sensor coil was also secured inside the needle shaft and very close to the tip in order to track the tip position at a rate of 25 Hz.

The robot is controlled using a proportional–integral–derivative (PID) controller in the joint space at a rate of 1 kHz while force/torque data are acquired at a rate of 200 Hz after being smoothed by a moving average filter. In order to reduce noise perturbation that is dominant at low velocities, which is the case in real interventions, a high-gain observer was implemented to estimate the velocity from encoder measurements. This system is capable of implementing more advanced approaches; however, it was employed here to validate the proposed modeling scheme.

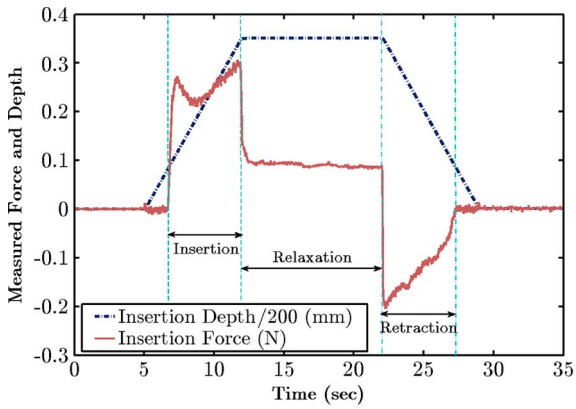

Fig. 3. Typical force and depth profiles during needle insertion into a homogeneous phantom (needle A/tissue A; $insertion\ velocity = 10$ mm/s).

Experiments were carried out on an artificial phantom made from Gelrite Gellan Gum (Sigma-Aldrich) with two concentration rates in water: 4.5% (tissue A; less stiff) and 6% (tissue B; more stiff). Based on our experiments and experience, this powder simulates a uniform elastic environment and mimics the frictional effects of biological tissues better than rubber phantoms. Compared to live tissues in which water comprises a considerable portion of the phantom, rubber-made artificial phantoms consist of a smaller number of water molecules, and that is why they generate an exaggerated amount of friction. The employed gum powder in this study created a more watery phantom that made the experiments more realistic in terms of the measured force ranges and viscosity. In order to get more consistent results, the room temperature must be controlled carefully. Keeping the phantom in the refrigerator for a few days leads to creating a thin crust on the tissue surface, which acts as a membrane. In our test bed, two sizes of stainless steel needle (Cook Medical) were used: the cannula of an 18GA needle (needle A; less flexible) with outer and inner diameters of 1.270 and 0.838 mm, respectively, and the cannula of a 22GA needle (needle B; more flexible) with outer and inner diameters of 0.718 and 0.413 mm, respectively.

B. Experimental Results

It is presumed that the insertion trajectory is of linear segment with parabolic blend (LSPB) with a preset velocity of the linear segment. The contact force was modeled under this constant speed assumption. Fig. 3 shows a sample of the recorded force and depth profiles. Note that, while exciting the system within a limited range of frequencies does not reveal all dynamic features, applying such a low-band signal was inevitable. Robot-assisted prostate brachytherapy entails a very similar insertion velocity profile, and one of our goals was to identify the force–depth parameters in a clinical condition.

Selecting the proper number of filters and state pairing are challenging tasks that affect the convergence rate, and a wrong selection can lead to instability in extreme cases. Based on our simulation studies and taking into account the observability properties of the system, three EKFs were employed in parallel according to the definitions given in Table I. It is notable that the reported results in this section are the outcomes of multiple

TABLE I
FILTER DEFINITION

applied model	filter number	$\tilde{\theta}_i$	$Q(\tilde{\theta}_i)$
I	$i=1$	(f_2,σ_0)	$0.05\times diag(10^5,10^9)$
	$i=2$	(f_1,σ_1)	$0.05\times diag(10^{15},10^{15})$
	$i=3$	(α,σ_2)	$0.05\times diag(10^5,10^{15})$
II	$i=1$	σ_0	0.05×10^9
	$i=2$	(f_1,σ_1)	$0.05\times diag(10^{15},10^{15})$
	$i=3$	(β,σ_2)	$0.05\times diag(10^3,10^{15})$

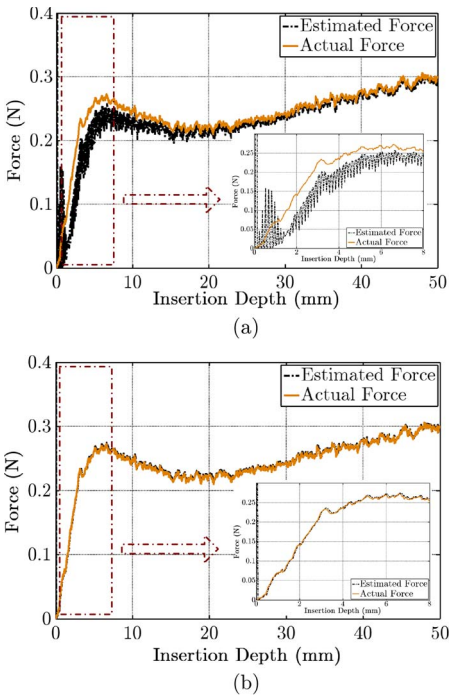

Fig. 4. Online force estimation during insertion using needle A/tissue A ($insertion\ velocity = 10$ mm/s). (a) Model I. (b) Model II.

experiments repeated under the same test conditions at different insertion points.

Each individual EKFs were tuned. To this effect, the initial error covariance matrices were chosen to be large in order to ensure rapid convergence. However, not much improvement was achieved for the diagonal magnitudes larger than 10^{15}. The system noise covariance matrices or $Q(\tilde{\theta}_i)$ representing the level of uncertainty in each subspace were set as in Table I in which index i refers to the subspace number. The measurement noise variance or R was also set to be 0.01 in each filter. This selection is a matter of a few trials and errors, and the noise patterns are assumed to be time invariant. In some studies, the initial values for the parameters are chosen very close to the estimated ones, although it is believed that this selection may result in an observability problem. In this paper, $\tilde{\phi}_0$ was set to be within $\pm 500\%$ of the estimated value of $\tilde{\phi}$ provided by the first run of the algorithm. Due to the highly nonlinear structure of the proposed model(s)/estimator, assuming a completely random initial state may result in either divergence or getting stuck in local minima.

Inserting the needle according to the profile shown in Fig. 3, the models introduced in Section III and in conjunction with the proposed online estimation technique exhibited the following

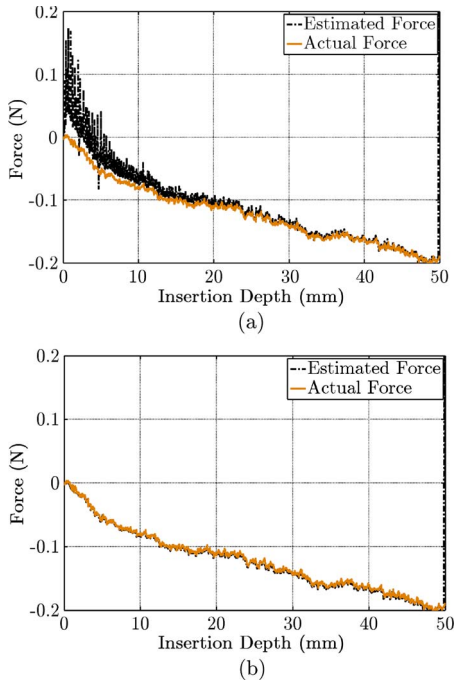

Fig. 5. Online force estimation during retraction using needle A/tissue A ($insertion\ velocity = 10$ mm/s). (a) Model I. (b) Model II.

performance. For this test, the combination of needle A plus tissue A was selected. Fig. 4 shows the estimated force during the insertion phase, while Fig. 5 shows the comparison of the estimated values and measured forces in the retraction stage. As shown in Fig. 4(a), the filter response is oscillatory, particularly during the prepuncture stage. Large transitions in the estimated values are also visible at the beginning of both insertion and retraction. Moreover, according to Fig. 5(a), during the retraction and in the vicinity of the entry point, model I exhibits poor estimation performance.

Root mean square error (rmse) is proposed here as a means of assessing the estimation quality. To this end, numerical results of the previous test are listed in Table II. The error values listed in the first half of the table include the entire insertion depth, while in the second half, the first five samples of both insertion and retraction data were intentionally ignored. Focusing more on the steady-state response, the second set of the reported values are therefore less affected by the initial oscillatory behavior of the estimator. Comparing the estimated signals shown in Figs. 4 and 5 and the numerical values reported in Table II verifies that model II outperforms model I.

As observed, the proposed scheme enables us to express the axial force during the needle–tissue interaction by estimating a set of parameters $(\tilde{\phi})$. As a rule of thumb, provided that the sequence of estimated values lies within the corresponding $\pm 3\sigma$ limits, the estimation is statistically confident, where σ denotes the standard deviation. Thus, to further investigate, a track of $\pm 3\sigma$ values was sequentially computed in each run.

Fig. 6 shows the estimated values for z, σ_2, σ_0, and f_2 of model I within the first 50 mm of insertion depth. Fig. 7 also shows the estimation results using model II in the same scenario at two examined speeds. Herein, σ_2, f_1, and β were selected for visualization. For the parameter α, it was noticed

TABLE II
RMSE OF THE PROPOSED ESTIMATOR (N)

including initial transition			
applied model	insertion phase	retraction phase	entire profile
I	1.68×10^{-1}	3.25×10^{-2}	1.21×10^{-1}
II	6.63×10^{-2}	2.09×10^{-2}	2×10^{-2}
excluding initial transition			
applied model	insertion phase	retraction phase	entire profile
I	1.81×10^{-2}	1.71×10^{-2}	2.03×10^{-2}
II	3.44×10^{-3}	2.83×10^{-3}	3.9×10^{-3}

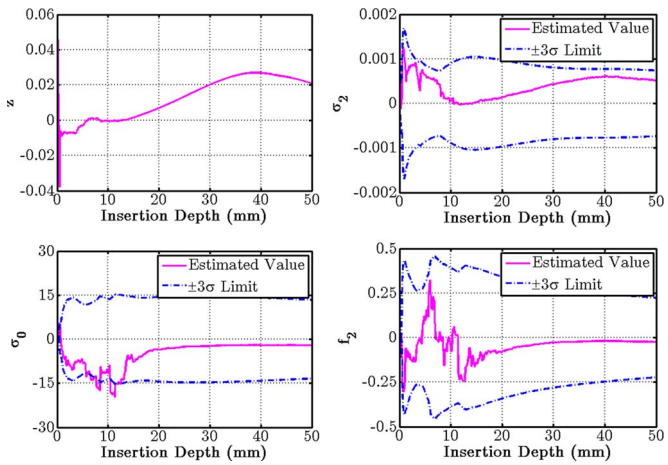

Fig. 6. State-parameter estimation during insertion using needle A/tissue A and model I ($insertion\ velocity = 10$ mm/s).

that, in the conducted experiments, the estimation starts to be dominated by noise from a middle point during the insertion process. Although being observable, the contribution of α in the model's output diminishes as the value of l increases, and this effect could not be improved by changing the associated noise parameter. Hence, to have less dependence on the noise characteristics, the value of α was assumed to be constant from the aforementioned point onward. This strategy resulted in more stable practical results; however, this observation led to adopting model II in which this parameter was omitted.

By comparison, estimation of σ_0 and σ_2 has the lowest confidence level and convergence rate, respectively, as shown in Fig. 6. In the same figure, rupture appears to be informative for the identification procedure, although inherent lack of excitation in the system avoids fast convergence. This problem can be partially resolved by injecting more noise into our state-space model that yields the selected $Q(\tilde{\theta})$ matrices in Table I. As emphasized previously, in order to have a realistic approach that can capture force–depth cycle during a clinical procedure, a low-velocity LSPB profile was applied. Note that needle insertion rates usually vary between 0.4 and 10 mm/s in clinical practice [9].

Next, the insertion velocity was reduced to 6 mm/s. As shown in Fig. 7 and in general, model II resulted in a more confident estimation in terms of retaining $\pm3\sigma$ limits at the lower examined velocity. To make a fair comparison, both filters were triggered from the same initial conditions. The force pattern relies on the insertion velocity; thus, the parameters

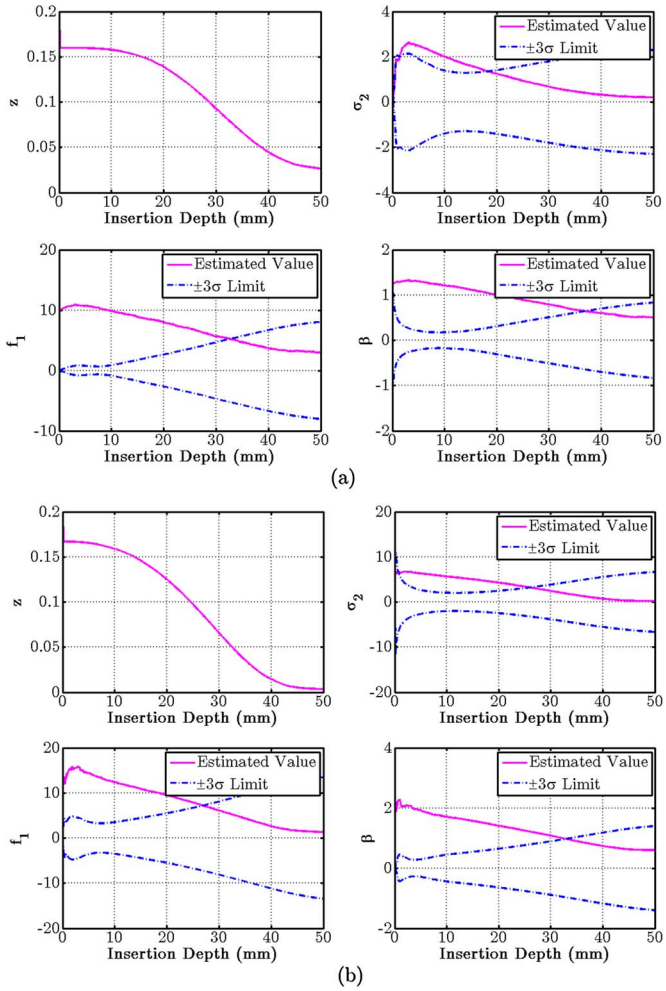

Fig. 7. State-parameter estimation during insertion using needle A/tissue A and model II. (a) $Insertion\ velocity = 10$ mm/s. (b) $Insertion\ velocity = 6$ mm/s.

settle down at different values at the end of the conducted experiments. As observed, the convergence rate and confidence level for a particular parameter are dependent on the velocity and the model employed, but model II outperforms model I according to Figs. 4 and 5.

For the final evaluation, model II was employed to simulate the force–length mapping using steady-state values of the parameters estimated in the previous step. Setting the speed to be 10 mm/s, the force profile was plotted using (3) and the following nominal values: $\sigma_0 = 7.9\times10^{-3}$, $\sigma_1 = 2.46$, $\sigma_2 = 4.14\times10^{-3}$, $f_1 = 5.59\times10^{-2}$, and $\beta = 2.55\times10^{-2}$. Note that the values of $\tilde{f}_2$ and $\tilde{\alpha}$ were already set to be -2.11×10^{-2} and 5.25×10^{-2}, respectively. The same simulation was repeated by plugging the following parameters into model II at 6 mm/s: $\sigma_0 = 3.91\times10^{-3}$, $\sigma_1 = 2.25$, $\sigma_2 = 3.55\times10^{-3}$, $f_1 = 3.25\times10^{-2}$, $\beta = 2.43\times10^{-2}$, $\tilde{f}_2 = -1.17\times10^{-2}$, and $\tilde{\alpha} = 3.63\times10^{-2}$.

It is evident from Fig. 8(a) and (b) that our strategy provides a means to capture the entire insertion–retraction loop without having *a priori* information about the phantom's biophysical properties, as well as the needle geometry. The mean absolute error values in the studied cases in Fig. 8 were calculated to be 9.87 and 7.52 mN, respectively.

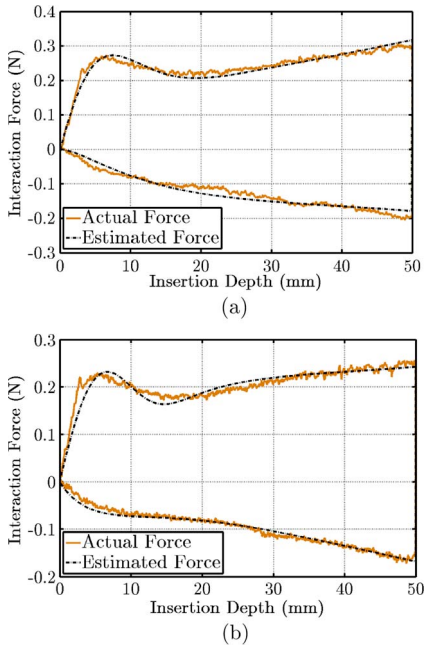

Fig. 8. Interaction force profile using model II, needle A/tissue A, and steady-state values of the estimated parameters. (a) $Insertion\ velocity = 10$ mm/s. (b) $Insertion\ velocity = 6$ mm/s.

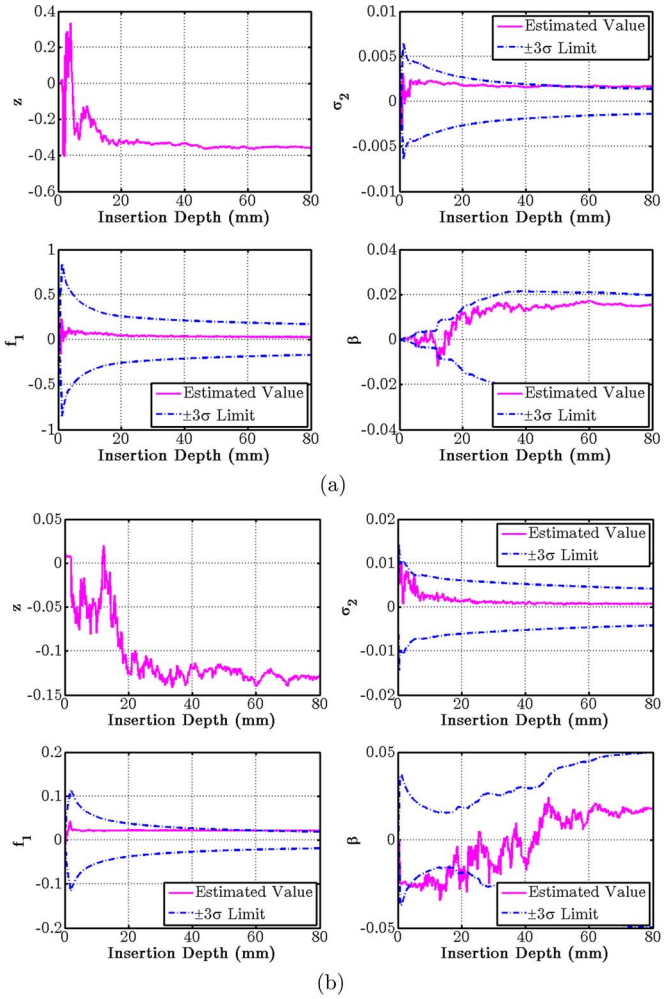

Fig. 9. State-parameter estimation during insertion using model II at 10 mm/s. (a) Needle B/tissue B. (b) Needle B/tissue A.

Now, in order to thoroughly evaluate the work, the same experiments were carried out for other needle–tissue combinations, i.e., needle A/tissue B, needle B/tissue A, and needle B/tissue B. Fig. 9 shows the parameter estimation using model II and the combination of needle B and tissue B during the 80 mm of insertion. Fig. 10 also shows the comparison of the measured force–depth cycles with the estimated ones using steady-state values of the estimated parameters, and Table III summarizes the steady-state parametric values in three sets of conducted experiments with the tinier needle. Inserting this needle at 6 mm/s was excluded from our studies due to the fact that force measurements were noisy and comparable to the force sensor's resolution. The existence of intricate friction in the internal structure of the robot, which is complex to be fully compensated for by the PID controller to provide a smooth motion, is a stumbling block using low-velocity profiles.

Note that the EM tracker measures the needle bending from its initial straight path. The inserted length of the needle is also known using forward kinematics of the robot. Thus, the inserted depth can be easily approximated and used in the force–depth model. In our experiments, the maximum deflection measured by the EM tracker at 50 mm of insertion depth for needle A/tissue A varied from 4.20 to 4.38 mm, whereas for the combination of needle B and tissue A, the deflection amount was limited to 6.62 mm.

As observed in Fig. 9(a) and (b), σ_2 and f_1 exhibited a marginal confidence level. In addition, apart from β whose convergence rate in both figures is relatively low, other parameters converged faster compared to the counterpart experiments performed with the 18GA needle. The mean absolutes of force estimation errors using steady-state parameters in the three studied cases shown in Fig. 10 were also 9.27, 9.41, and 11.02 mN, respectively. It is worthwhile noting that, in practice, it was not easy to make a purely homogeneous phantom using gum powder. There always existed some air bubbles in the entire volume of the phantom, which prevented the elastic medium from being completely uniform and added unexpected force oscillations to the measured data set. Due to the lower stiffness (or greater flexibility) of the 22GA needle compared to the 18GA one, needle B was susceptible to the effect of air bubbles, as observed in our experiments.

To conclude, the proposed online mechanism for tuning the filter allows us to minimize the error between the measured and the estimated axial force instead of accurate parameter estimation. In other words, even in a homogeneous environment, the estimated coefficients can be slightly different, depending on the maximum penetration depth or applied trajectory. A critical point that has to be noticed is that the convergence rate of each parameter relies on a variety of factors, including insertion velocity, state pairing, initial adjustment, and the selected needle–tissue combination.

To illustrate this fact, the initial value of f_2 in the experiments using needle A/tissue A combination was switched to -0.01 instead of 0.01. For a long insertion depth at 10 mm/s, the filter tended to be unstable. Then, σ_0 and σ_2 in model II were paired together, and β was treated as a single parameter in

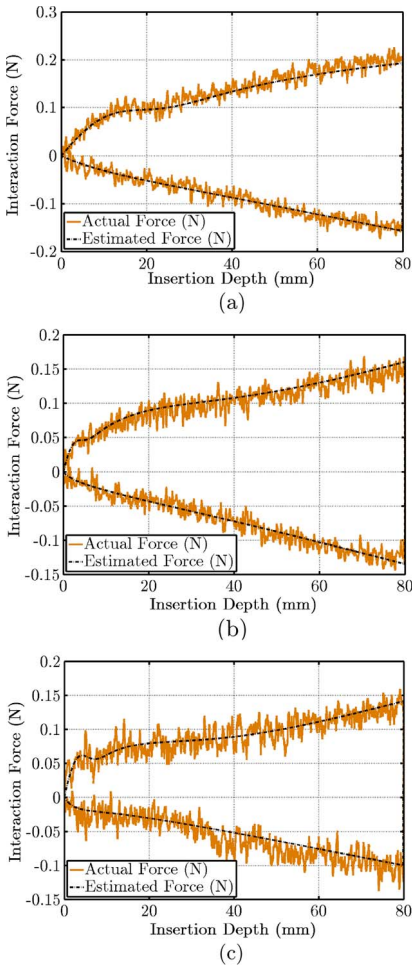

Fig. 10. Interaction force profile using model II, and steady-state values of the estimated parameters. (a) Needle B/tissue B; $insertion\ velocity = 10$ mm/s. (b) Needle B/tissue B; $insertion\ velocity = 6$ mm/s. (c) Needle B/tissue A; $insertion\ velocity = 10$ mm/s.

the filter bank, as opposed to our initial setting described in Table I. As the results confirmed, the convergence was very slow and considerably dominated by the system noise. Note that it is a complex task to draw a solid conclusion on the model's sensitivity with respect to the initial value selection. Therefore, achieving optimal performance and improving the convergence rate and robustness require a more intricate strategy to tune the bank of filter, and this is left for future work. In general, optimal tuning can be a complicated task in estimation theory, and it is an area of challenge.

VI. Conclusion and Future Work

In this paper, the application of asynchronous joint EKF in needle insertion has been studied. In summary, it is a complex task to find an explicit mapping between existing variables and measured force profile during needle–tissue interaction, and the sheer complexity of the physics behind it led us to seek a non-physics-based approach. Most of the current models reported in the literature are not implementable in operating conditions. For instance, while FEM is well suited to compute accurate and complex deformation of soft tissue, it is difficult to achieve a perfect real-time performance even on a moderately powerful workstation [1], [16]. From this point of view, successful parameter identification from intraoperative data stream during a conventional medical procedure is a remarkable advantage.

TABLE III
Steady-State Values of the Estimated Parameters Using Model II and Needle B

	tissue B v=10 mm/s	tissue B v=6 mm/s	tissue A v=10 mm/s
σ_0	9.2×10^{-4}	8.37×10^{-4}	7.96×10^{-4}
σ_1	4.48×10^{-1}	9.27×10^{-1}	5.35×10^{-1}
σ_2	1.63×10^{-3}	1.79×10^{-3}	7.63×10^{-4}
f_1	2.7×10^{-2}	9.21×10^{-3}	2.15×10^{-2}
$\tilde{f}_2$	-9.96×10^{-3}	2.49×10^{-1}	-1.19×10^{-2}
$\tilde{\alpha}$	1.11×10^{-2}	5.84×10^{-2}	1.08×10^{-2}
β	1.53×10^{-2}	1.36×10^{-2}	1.58×10^{-2}

This study presented a method that is particularly important for needle-based interventions performed using a robotic system, where no imaging data are available throughout the operation. As the needle interacts with an elastic medium, the force–depth measurements provide a useful guide to characterize force evolution. The axial interaction force was described using a nonlinear state-space model, and associated parameters were intraoperatively identified. Hence, explicit knowledge of needle and tissue properties was not required prior to experimentations. Another achievement in our study was to describe the entire axial force without performing the following: 1) separating the measured force to its constituent components, including rupture, friction, and cutting forces, and 2) using preoperative curve fitting or least squares methods. Although existing parameters in this model cannot be intuitively interpreted, the presented single-state model holds appeal due to its simplicity and real-time implementation. From the experiments, we can conclude that the proposed modeling strategy is feasible and efficient. Consequently, it is possible to make an atlas for a variety of needle–tissue combinations and then take advantage of the proposed scheme in the absence of the force/torque sensor in order to have an approximation of the total translational force.

We plan to investigate the performance of our scheme using a multilayer phantom which mimics the behavior of a live tissue during percutaneous therapies. To this end, each layer consisting of a membrane plus a rigid body can be represented by the proposed model and a set of parameters in the force domain. Model validation during *in vivo* experiments and in the presence of vascular pressure and temperature effects is left for future work. Finally, our ongoing work is concerned with the integration of the force estimator with a steering mechanism to provide more accuracy and robustness. In [2] and [3], while assuming a constant radius of curvature for steering, no force feedback was utilized to update the needle curvature. Applying an adaptive approach can be the first step to enhance the overall performance in robot-assisted needle insertion or force control in a haptic system.

Acknowledgment

The development of the robotic system for prostate brachytherapy was also supported by Natural Sciences and Engineering Research Council (NSERC) and Canadian Institutes

of Health Research (CIHR) under the NSERC Collaborative Health Research Project Grant 262583-2003 (R. V. Patel, Principal Investigator) and by infrastructure grants from the Canada Foundation for Innovation awarded to the London Health Sciences Centre and to The University of Western Ontario.

REFERENCES

[1] N. Abolhassani, R. Patel, and M. Moallem, "Needle insertion into soft tissue: A survey," *Med. Eng. Phys.*, vol. 29, no. 4, pp. 413–431, Mar. 2007.

[2] K. B. Reed, V. Kallem, R. Alterovitz, K. Goldberg, A. M. Okamura, and N. J. Cowan, "Integrated planning and image-guided control for planar needle steering," in *Proc. 2nd Biennial IEEE/RAS-EMBS Int. Conf. Biomed. Robot. Biomechatron.*, 2008, pp. 819–824.

[3] A. Asadian, M. R. Kermani, and R. V. Patel, "Robot-assisted needle steering using a control theoretic approach," *J. Intell. Robot. Syst.*, vol. 62, no. 3/4, pp. 397–418, Jun. 2011.

[4] P. L. Yen, R. Hibberd, and B. Davies, "A telemanipulator system as an assistant and training tool for penetrating soft tissue," *Mechatronics*, vol. 6, no. 4, pp. 377–489, 1996.

[5] A. M. Okamura, C. Simone, and M. D. O'Leary, "Force modeling for needle insertion into soft tissue," *IEEE Trans. Biomed. Eng.*, vol. 51, no. 10, pp. 1707–1716, Oct. 2004.

[6] P. N. Brett, A. J. Harrison, and T. A. Thomas, "Schemes for the identification of tissue types and boundaries at the tool point for surgical needles," *IEEE Trans. Inf. Technol. Biomed.*, vol. 4, no. 1, pp. 30–36, Mar. 2000.

[7] T. K. Podder, J. Sherman, E. M. Messing, D. J. Rubens, D. Fuller, J. G. Strang, R. A. Brasacchio, and Y. Yu, "Needle insertion force estimation model using procedure-specific and patient-specific criteria," in *Proc. 28th IEEE EMBS Annu. Int. Conf.*, 2006, pp. 555–558.

[8] T. K. Podder, J. Sherman, D. Fuller, E. M. Messing, D. J. Rubens, J. G. Strang, R. A. Brasacchio, and Y. Yu, "*In-vivo* measurement of surgical needle intervention parameters: A pilot study," in *Proc. 28th IEEE EMBS Annu. Int. Conf.*, 2006, pp. 3652–3655.

[9] S. P. DiMaio and S. E. Salcudean, "Needle insertion modeling and simulation," *IEEE Trans. Robot. Autom.*, vol. 19, no. 5, pp. 864–875, Oct. 2003.

[10] J. T. Hing, A. D. Brooks, and J. P. Desai, "Reality-based estimation of needle and soft-tissue interaction for accurate haptic feedback in prostate brachytherapy simulation," *Robot. Res.*, vol. 28, *Springer Tracts Advanced Robotics*, pp. 34–48, 2007.

[11] S. Misra, K. B. Reed, A. S. Douglas, K. T. Ramesh, and A. M. Okamura, "Needle–tissue interaction forces for bevel-tip steerable needles," in *Proc. 2nd Biennial IEEE/RAS-EMBS Int. Conf. Biomed. Robot. Biomechatron.*, 2008, pp. 224–231.

[12] Y. Kobayashi, A. Onishi, H. Watanabe, T. Hoshi, K. Kawamura, and M. G. Fujie, "*In vitro* validation of viscoelastic and nonlinear physical model of liver for needle insertion simulation," in *Proc. 2nd Biennial IEEE/RAS-EMBS Int. Conf. Biomed. Robot. Biomechatron.*, 2008, pp. 469–476.

[13] M. H. Lu, W. Yu, Q. H. Huang, Y. P. Huang, and Y. P. Zheng, "A handheld indentation system for the assessment of mechanical properties of soft tissues *in vivo*," *IEEE Trans. Instrum. Meas.*, vol. 58, no. 9, pp. 3079–3085, Sep. 2009.

[14] K. G. Yan, T. Podder, Y. Yu, T. Liu, and C. W. S. Cheng, "Flexible needle–tissue interaction modeling with depth-varying mean parameter: Preliminary study," *IEEE Trans. Biomed. Eng.*, vol. 56, no. 2, pp. 255–262, Feb. 2009.

[15] L. Barbe, B. Bayle, and M. de Mathelin, "*In vivo* model estimation and haptic characterization of needle insertions," *Int. J. Robot. Res.*, vol. 26, no. 11/12, pp. 1283–1301, Nov. 2007.

[16] S. Misra, K. T. Ramesh, and A. M. Okamura, "Modeling of tool–tissue interactions for computer-based surgical simulation: A literature review," *Presence-Teleop. Virt.*, vol. 17, no. 5, pp. 463–491, Oct. 2008.

[17] J. T. Hing, A. D. Brooks, and J. P. Desai, "A biplanar fluoroscopic approach for the measurement, modeling, and simulation of needle and soft-tissue interaction," *Med. Image Anal.*, vol. 11, no. 1, pp. 62–78, Feb. 2007.

[18] H. Delingette, "Towards realistic soft-tissue modeling in medical simulation," *Proc. IEEE—Special Issue on Surgery Simulation*, vol. 85, no. 3, pp. 512–523, Mar. 1998.

[19] M. R. Kermani, R. V. Patel, and M. Moallem, "Friction identification and compensation in robotic manipulators," *IEEE Trans. Instrum. Meas.*, vol. 56, no. 6, pp. 2346–2353, Dec. 2006.

[20] A. Asadian, M. R. Kermani, and R. V. Patel, "A compact dynamic force model for tissue–needle interaction," in *Proc. 32nd IEEE EMBS Annu. Int. Conf.*, 2010, pp. 2292–2295.

[21] L. R. Ray, A. Ramasubramanian, and J. Townsend, "Adaptive friction compensation using extended Kalman–Bucy filter friction estimation," *Control Eng. Pract.*, vol. 9, no. 2, pp. 169–179, Feb. 2001.

[22] P. Lichinsky, C. Canudas De Wit, and G. C. Morel, "Friction compensation for an industrial hydraulic robot," *IEEE Control Syst.*, vol. 19, no. 1, pp. 25–32, Feb. 1999.

[23] C. K. Chui and G. Chen, *Kalman Filtering With Real-Time Applications*, 4th ed. Berlin, Germany: Springer-Verlag, 2008.

[24] P. Moireau, D. Chapelle, and P. L. Tallec, "Joint state and parameter estimation for distributed mechanical systems," *Comput. Methods Appl. Mech. Eng.*, vol. 197, no. 6–8, pp. 659–677, Jan. 2008.

[25] L. P. Yan, B. S. Liu, and D. H. Zhou, "The modeling and estimation of asynchronous multirate multisensor dynamic systems," *Aerosp. Sci. Technol.*, vol. 10, no. 1, pp. 63–71, Jan. 2006.

[26] H. S. Bassan, R. V. Patel, and M. Moallem, "A novel manipulator for percutaneous needle insertion: Design and experimentation," *IEEE/ASME Trans. Mechatron.*, vol. 14, no. 6, pp. 746–761, Dec. 2009.

Ali Asadian (S'10) received the B.Sc. degree in electrical engineering/control systems from Sharif University of Technology, Tehran, Iran, in 2002 and the M.Sc. degree in electrical engineering/control systems from the University of Tehran, Tehran, in 2005. Since 2008, he has been working toward the Ph.D. degree at The University of Western Ontario, London, ON, Canada.

He is currently a Natural Sciences and Engineering Research Council Computer-Assisted Medical Interventions Program Scholar and is working with the Canadian Surgical Technologies and Advanced Robotics, Lawson Health Research Institute, London, Canada, as a Research Assistant. His current research interests include surgical needle insertion/steering, medical robotics, and control theory with applications to minimally invasive surgery.

Mehrdad R. Kermani (M'05) received the B.Sc. degree in electrical and computer engineering from Isfahan University of Technology, Isfahan, Iran, in 1994, the M.Sc. degree in electrical and computer engineering from Iran University of Science and Technology, Tehran, Iran, in 1997, and the Ph.D. degree in electrical and computer engineering from The University of Western Ontario, London, ON, Canada, in 2005.

From 1997 to 2001, he was a Senior Automation Consultant in the field of steel industries. He is currently an Assistant Professor with the Department of Electrical and Computer Engineering, The University of Western Ontario, and a Senior Scientist with the Canadian Surgical Technologies and Advanced Robotics, Lawson Health Research Institute, London, Canada. His research interests include human-safe robotic systems, smart materials, medical robotics, and structural flexibilities.

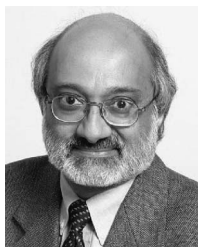

Rajni V. Patel (M'76–SM'80–F'92) received the Ph.D. degree in electrical engineering from the University of Cambridge, Cambridge, U.K., in 1973.

He is currently a Distinguished University Professor and the Tier-1 Canada Research Chair with the Department of Electrical and Computer Engineering, with a cross-appointment in the Department of Surgery, Schulich School Medicine and Dentistry, The University of Western Ontario, London, ON, Canada. He is also the Director of Engineering for the Canadian Surgical Technologies and Advanced Robotics, Lawson Health Research Institute, London, Canada. He is currently a Member of the Advisory Board of the *International Journal of Medical Robotics and Computer Assisted Surgery*.

Dr. Patel is a fellow of the American Society of Mechanical Engineers (ASME), the Royal Society of Canada, and the Canadian Academy of Engineering. He has served on the editorial boards of the IEEE TRANSACTIONS ON ROBOTICS, the IEEE/ASME TRANSACTIONS ON MECHATRONICS, and the IEEE TRANSACTIONS ON AUTOMATIC CONTROL.